# CONFERENCE PRE-PRINT

# NUMERICAL SIMULATION OF EFFECT OF POLOIDAL INJECTION GEOMETRY ON LI-PELLET TRIGGERED ELM UNDER BOUT++ FRAMEWORK

#### M. Li

Key Laboratory of Materials Modification by Laser, Ion, and Electron Beams (Minister of Education), School of Physics, Dalian University of Technology Dalian, People's Republic of China

Email: maoli ganf@outlook.com

#### T.Y. Xia

Institute of Plasma Physics, Chinese Academy of Sciences Hefei, People's Republic of China

#### Z. Sun

Princeton Plasma Physics Laboratory Princeton, United States of America

#### H.Y. Chang

Key Laboratory of Materials Modification by Laser, Ion, and Electron Beams (Minister of Education), School of Physics, Dalian University of Technology Dalian, People's Republic of China

# J.Z. Sun

Key Laboratory of Materials Modification by Laser, Ion, and Electron Beams (Minister of Education), School of Physics, Dalian University of Technology Dalian, People's Republic of China

Email: jsun@dlut.edu.cn

### **Abstract**

A BOUT++ three-field MHD code coupled with an impurity model has been employed to investigate the physical processes of ELM triggering by lithium pellet injection from the poloidal positions of low-field-side X-point (scenario LFS-X-point) and high-field-side X-point (scenario HFS-X-point), respectively. It is found that the ELM triggering threshold for injection from HFS X-point is smaller than that for injection from LFS X-point. The result is consistent with a previous JOREK simulation of deuterium pellet triggering ELM [Futatani S. et. Al., Nucl. Fusion, 54, 073008, 2014]. In addition, unlike scenario LFS-X-point, in scenario HFS-X-point there exhibits a broad parameter window for small pellet sizes, under which the triggered ELM size is only about 0.1%. This highlights a unique advantage of high-field-side pellet injection in ELM control. Furthermore, the characteristics of pellet-triggered ELMs vary significantly with the poloidal injection position. In scenario LFS-X-point, the triggered ELM undergoes phases of fast crash, turbulent transport, and saturation. In contrast, in scenario HFS-X-point, it is found that the nonlinear dominant mode can be rapidly suppressed to a very low level, making the fast crash phase negligible. As a result, the triggered ELM in this scenario exhibits turbulent characteristics. The present study is expected to provide a physical basis for choosing the poloidal geometry of pellet injection in future experiments.

# 1. INTRODUCTION

Edge Localized Modes (ELMs) are commonly observed at the plasma boundary under high-confinement mode (H-mode) operation in fusion devices [1]. Although ELMs facilitate the expulsion of excess particles and impurities from the core through the edge transport barrier [2], which is beneficial for steady-state operation, the associated high transient heat fluxes can cause severe material damage and reduce the lifetime of plasma-facing components (PFCs), especially the divertor targets [3]. Therefore, effective control of ELMs is crucial for achieving long-pulse, high-performance steady-state operation in future low-collisionality burning plasma tokamaks.

Pellet injection has been demonstrated in multiple devices to effectively regulate ELMs by increasing their frequency and reducing their amplitude, whether using deuterium (D) pellets or impurity pellets [4-9]. However, deuterium pellet injection increases the total fuel throughput of the vessel, which will be constrained by the

capacity of pumping and tritium processing systems in future reactors [10]. Thus, impurity pellet injection remains a candidate scheme for active ELM control in future device operations, as it decouples ELM pacing and fuelling. Previous impurity pellet injection experiments were mainly conducted on the EAST and DIII-D devices [7-9,11-13], among which lithium (Li) pellet injection has attracted significant attention. Sub-millimeter lithium pellets have been used in EAST experiments to successfully achieve active control of high-frequency natural ELMs; by varying the pellet size and injection frequency in real time, threshold behaviour in the pellet ELM triggering process was identified, and probabilistic triggering characteristics were observed when the injected pellet size was below the threshold [7-8]. This phenomenon has also been observed in DIII-D experiments, where it was found that the transient heat flux deposition on the inner and outer divertor targets could be effectively mitigated during ELM pacing [9].

Extensive simulations have also been conducted to explore the physical mechanisms underlying the pellet ELM triggering process. To describe the pellet ablation and homogenization processes, several models have been developed over the past decades [14-16]. Among these models, a hybrid model [15] has been coupled into the JOREK code to further investigate the characteristics of D-pellet triggered ELMs and their dependence on pellet injection parameters [17-20]. In the field of impurity pellet injection, the transport code SOLPS coupled with a dynamical Neutral Gas Shielding (NGS) model [16] has been employed to simulate the transport of Li ions and the evolution of background plasma profiles during Li pellet injection experiments on EAST [21]. Based on the previous SOLPS work, the threshold behaviour of pellet ELM triggering in EAST experiments was successfully reproduced by using a BOUT++ three-field MHD code, and the effect of radial deposition location on ELMs had been also discussed [22]. Moreover, through the development of an impurity model, our previous BOUT++ simulations enabled an in-depth study of the physical processes of ELM triggering by Li pellets [23].

However, compared with D pellet injection, the understanding of the physical mechanisms behind impurity pellet triggering ELM remains insufficient. To date, previous experiments and simulations have not investigated the effect of poloidal injection geometry on the ELM triggering process by impurity pellet. Given that the planned poloidal injection position for ITER is near the X-point [17], systematic simulation on this issue is necessary, which is the focus of the present work. Besides, a previous JOREK simulation found that the size threshold for ELM triggering by D pellets under different poloidal injection geometries contradicted conventional understanding: the threshold was lowest when injected from the high-field side (HFS), intermediate from the low-field side (LFS) X-point, and highest from the outer midplane (OMP) [17]. However, the JOREK study did not provide an in-depth analysis of the underlying mechanisms. The findings of this paper can address this gap. The present work is the follow-up of [23]. In [23], we investigated the threshold behaviour and subsequent evolution of ELM triggering by Li pellets injected from OMP. This paper further extends the study to other scenarios including injection from the LFS X-point and the HFS X-point, aiming to reveal the effect of poloidal injection geometry on Li pellet triggering ELM.

The remaining parts of this paper are organized as follows: the physical model and simulation setup are presented in Section 2; the results are reported in Section 3; and the conclusions and discussions are summarized in Section 4.

# MODEL AND SIMULATION SETUP

A BOUT++ three-field MHD code coupled with an impurity model [23] is employed here to investigate the triggering and subsequent evolution of ELMs following Li pellet injection from different poloidal positions under the EAST experimental configuration. The model evolves three perturbed physical quantities: vorticity  $\varpi$ , pressure P, and parallel vector potential  $A_{\parallel}$ . After incorporating peeling-ballooning modes (PBMs), ion diamagnetic drift, electric drift, gyro-viscosity, resistivity, anomalous electron viscosity and impurity equilibrium effects, the governing equations of the MHD model are expressed as follows:

$$\frac{\partial w}{\partial t} + \boldsymbol{v}_{\mathbf{E}} \cdot \boldsymbol{\nabla} \boldsymbol{\varpi} = B_{0} \boldsymbol{\nabla}_{\parallel} \boldsymbol{J}_{\parallel} + 2\boldsymbol{b}_{0} \times \boldsymbol{\kappa}_{0} \cdot \boldsymbol{\nabla} P 
- \frac{1}{2\Omega_{\mathbf{i}}} \left[ Z_{\mathbf{i}} e n_{\mathbf{i},0} \boldsymbol{v}_{\mathbf{D}\mathbf{i}} \cdot \boldsymbol{\nabla} (\boldsymbol{\nabla}_{\perp}^{2} \boldsymbol{\Phi}) - \boldsymbol{v}_{\mathbf{E}} \cdot \boldsymbol{\nabla} (\boldsymbol{\nabla}_{\perp}^{2} P_{\mathbf{i}}) + \boldsymbol{\nabla}_{\perp}^{2} (\boldsymbol{v}_{\mathbf{E}} \cdot \boldsymbol{\nabla} P_{\mathbf{i}}) \right], 
- \frac{1}{2\Omega_{\mathbf{i}\mathbf{m}}} \left[ Z_{\mathbf{i}} e n_{\mathbf{i}\mathbf{m},0} \boldsymbol{v}_{\mathbf{D}\mathbf{i}\mathbf{m},0} \cdot \boldsymbol{\nabla} (\boldsymbol{\nabla}_{\perp}^{2} \boldsymbol{\Phi}) - \boldsymbol{v}_{\mathbf{E}} \cdot \boldsymbol{\nabla} (\boldsymbol{\nabla}_{\perp}^{2} P_{\mathbf{i}\mathbf{m},0}) + \boldsymbol{\nabla}_{\perp}^{2} (\boldsymbol{v}_{\mathbf{E}} \cdot \boldsymbol{\nabla} P_{\mathbf{i}\mathbf{m},0}) \right]$$
(1)

$$\frac{\partial P}{\partial t} + \boldsymbol{v}_{\mathbf{E}} \cdot \boldsymbol{\nabla} P = 0, \tag{2}$$

$$\frac{\partial A_{\parallel}}{\partial t} = -\nabla_{\parallel} \Phi + \frac{\eta}{\mu_0} \nabla_{\perp}^2 A_{\parallel} - \frac{\eta_{\rm H}}{\mu_0} \nabla_{\perp}^4 A_{\parallel}. \tag{3}$$

In equations (1~3), all quantities consist of equilibrium and perturbed components, which can be represented as  $F = F_0 + F_1$ . In this model,  $\varpi = \frac{n_{i,0}m_i}{B_0} \left( \nabla_\perp^2 \phi + \frac{1}{n_{i0}} \nabla n_{i,0} \cdot \nabla \phi + \frac{1}{n_{i,0}Z_{ie}} \nabla_\perp^2 P_{i,1} \right) + \frac{m_{im}n_{im,0}}{B_0} \left( \nabla_\perp^2 \phi + \frac{1}{n_{im,0}} \nabla_\perp \phi \cdot \nabla_\perp \phi \right)$ ,  $V_{\perp} = V_{\perp} = V_{$ 

In this study, the total equilibrium pressure is defined as  $P_0 = P_{i,0} + P_{e,0} + P_{im,0}$ , which is modified by the impurity equilibrium pressure. In addition, the relationships between the other impurity equilibria and the background plasma equilibria are  $T_{im,0} = T_{i,0}$  and  $n_{im,0} = \Delta P_{\rm p}/(Z_{im}T_{\rm e,0} + T_{i,0})$ , respectively. Here, the quantity  $\Delta P_{\rm p}$  describes the pressure perturbation introduced by Li pellet injection, and its expression is given by:

$$\Delta P_{\rm p} = P_{\rm height} \times e^{-\left(\frac{x - x_{\rm center}}{x_{\rm width}}\right)^2} \times e^{-\left(\frac{y - y_{\rm center}}{y_{\rm width}}\right)^2}, \tag{4}$$

where  $P_{\text{height}}$  is the amplitude of  $\Delta P_{\text{p}}$ ; x is a normalized poloidal magnetic flux and y is a parameter to represent the poloidal position; the dimensionless parameters  $x_{\text{width}}$ ,  $x_{\text{center}}$  and  $y_{\text{width}}$ ,  $y_{\text{center}}$  are used to control the width and the peak position of  $\Delta P_{\text{p}}$  profile in the radial and poloidal directions, respectively. In this work, the parameter  $Z_{\text{im}}$  is the effective charge number and its value is set to be three for Li impurity.

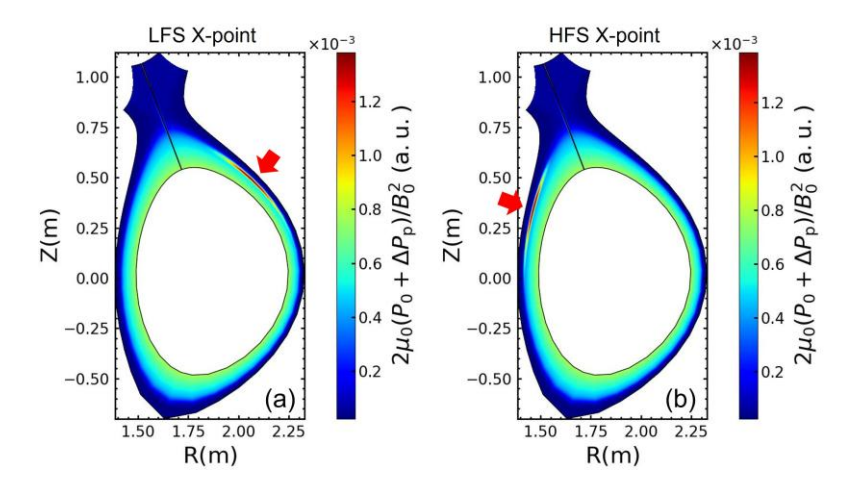


Fig. 1. Diagram of poloidal injection geometries in scenarios (a) LFS X-point and (b) HFS X-point.

The present paper simulates scenarios in which the pellets are injected from two poloidal positions: the low-field-side X-point (scenario LFS-X-point) and the high-field-side X-point (scenario HFS-X-point), with a schematic provided in Fig. 1. A previous JOREK simulation [17] showed that for a pellet of identical size and injection speed, which is capable of triggering ELMs, the radial extent of the locally enhanced pressure profile introduced by pellet ablation is broadest when injected from the outer midplane (scenario OMP), intermediate for injection from the LFS X-point, and narrowest for injection from the HFS. Moreover, as the pellet injection position shifts from OMP to HFS, the radial position of the pressure perturbation peak gradually moves toward the plasma edge. Based on the findings, the radial parameters  $x_{center}$  and  $x_{width}$  in Equation (4) are set to 0.956 and 0.016 for scenario LFS-X-point and to 0.975 and 0.011 for scenario HFS-X-point (in our previous work [23], the scenario OMP uses  $x_{center} = 0.937$  and  $x_{width} = 0.021$ ), thereby describing the radial pressure perturbation profiles induced by pellet injection in corresponding scenarios. Besides, as the previous SOLPS and JOREK simulations [17, 21] both suggested that the locally enhanced radial pressure peak following pellet injection is a critical parameter for ELM triggering, the cases with similar initial local pressure peaks after pellet injection are then compared between the two scenarios in this work, i.e., those represented by curves of the same color in Fig. 2.

Besides, considering that in the present simulation the number of poloidal grid points near the X-point region is approximately 1.5 times that at the outer midplane, the poloidal parameter  $y_{\text{width}}$  in Equation (4) is set to 0.2 for scenarios LFS-X-point and HFS-X-point to ensure that the primarily Li-ions-affected region along the poloidal direction determined by the pressure perturbation  $\Delta P_{\text{p}}$  remains consistent with that of scenario OMP in [23], where  $y_{\text{width}}$  is set to 0.3. Furthermore, the other BOUT++ simulation settings, as well as the EAST equilibrium and the pellet ELM triggering model used in this study are both identical to those in our previous work. For more details, refer to [23].

#### 3. SIMULATION RESULT

In this work, the nonlinear simulations, which consider the interactions between n = 0, 5, 10, 15, 20, 25, 30, 35, 40 modes, are performed to investigate the physical mechanisms behind ELM triggering when lithium pellets are injected from the low-field-side X-point and the high-field-side X-point, respectively. the toroidal mode numbers n of the modes with the highest linear growth rates were found to be 5, 5, and 10 for the cases of  $R_p = 2.1, 2.8,$  and 3.5 in scenario LFS-X-point; whereas for the cases of  $R_p = 4.6$  and 5.7 in scenario HFS-X-point, the toroidal mode numbers were both 5. Hereafter, the mode with the highest linear growth rate in each case of the two scenarios is defined as the linear dominant mode, and the mode characterized by rapid growth of perturbation amplitude in nonlinear simulations that ultimately triggers an ELM is defined as the nonlinear dominant mode. the parameter  $R_p$  is defined as the rate of the modified pressure over the unperturbed one at the radial peak deposition position (i.e.,  $R_p = P_{\text{mod,PDP}}/P_{0,\text{PDP}}$  where PDP stands for peak deposition position), which is used to represent the pellet deposition amount in a given scenario [22-23]. The time step  $\tau_A$  is 0.47  $\mu$ s for every case.

# 3.1. Pedestal energy loss

Fig. 2 shows the time evolution of the ELM size for the cases in scenarios LFS-X-point and HFS-X-point, respectively. For the definition of ELM size please refer to [23]. As can be seen from Fig. 2(a), for scenario LFS-X-point, no pedestal energy loss is observed within the whole simulation time when  $R_p = 1.4$ . When  $R_p > 1.4$ , it can be seen that the injected pellets can both trigger ELMs with significant amplitude, whose evolution after ELM onset consists of the phased of fast crash, turbulent transport and saturation. Moreover, it is observed that as  $R_p$  increases, the time point of ELM onset gradually decreases to around  $t = 180 \ \tau_A$ .

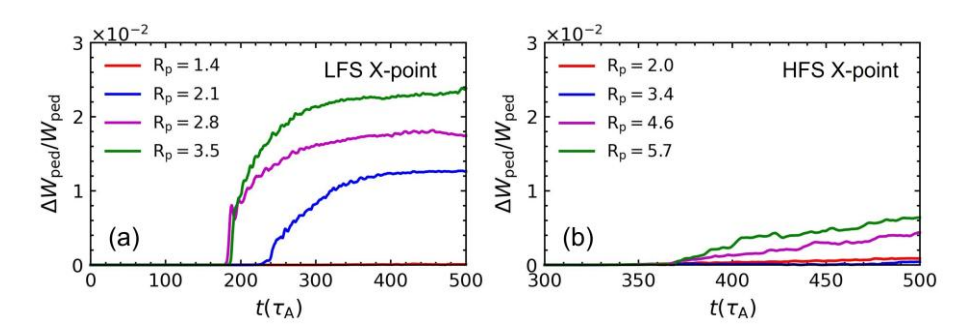


Fig. 2. Time evolutions of ELM sizes in scenarios (a) LFS-X-point and (b) HFS-X-point.

In contrast, when Li pellets are injected from HFS X-point (scenario HFS-X-point), the evolutionary characteristics of the triggered ELMs are very different from those in scenario LFS-X-point. As shown in Fig. 2(b), although pellet injection still induces pedestal energy loss even in the smallest  $R_p$  case, the fast crash phase of the ELM evolution is negligible. Namely, the triggered ELMs almost directly enter and remain in a turbulent transport phase with low energy loss rate, resembling the turbulent crash mentioned in [29]. Furthermore, the time points of ELM onset in the cases of scenario HFS-X-point are both much larger than those in scenario LFS-X-point, all exceeding 360  $\tau_A$ . Under these conditions, the ELM sizes in the former are significantly smaller than those in the latter.

#### 3.2. Toroidal components of pressure perturbation

To better understand the process of nonlinear ELM evolution induced by Li pellet injection from different poloidal positions, we take a look at the time evolutions of the on-resonant toroidal components ( $n \neq 0$ ) of pressure perturbation after pellet injection. The data of scenarios LFS-X-point and HFS-X-point are chosen, respectively,

from the positions of the negative and positive extrema of the radial pressure gradient at the poloidal injection position. The results are depicted in Fig. 3. The insets in this figure include the period near ELM onset. The red dashed lines represent the time points of ELM onset, which are obtained based on the data of Fig. 2. It is clearly seen from Fig. 3 (a~c) that when lithium pellets are injected from the LFS X-point, in the case of  $R_p$  =2.1, no other mode grows to become a nonlinear dominant mode with amplitude comparable to the dominant n = 5 mode before ELM onset. Moreover, the n = 5 mode does not undergo a secondary growth after ELM onset; instead, it decays slowly with oscillations during the fast crash phase. This behavior differs from the characteristics of turbulent ELMs mentioned in [23] but is closer to a conventional ELM crash. Only when  $R_p$  is increased to 2.8 can the secondary growth of the nonlinear dominant n = 5 mode be observed. When Rp is further increased to 3.5, the linearly dominant n = 10 mode and the n = 5 mode (whose linear growth rate is similar to that of n = 10 mode) can grow fast together and jointly trigger a turbulent ELM. Besides, both of the two modes are observed to experience a secondary growth after ELM onset. These results are consistent with those in our previous work in which the pellet is injected from the poloidal position of OMP [23]. Furthermore, because of the secondary growth of nonlinear dominant modes, the corresponding pedestal energy losses during the fast crash phase in the cases of  $R_p = 2.8$  and 3.5 are more pronounced than that when  $R_p = 2.1$ , as shown in Fig. 2(a).

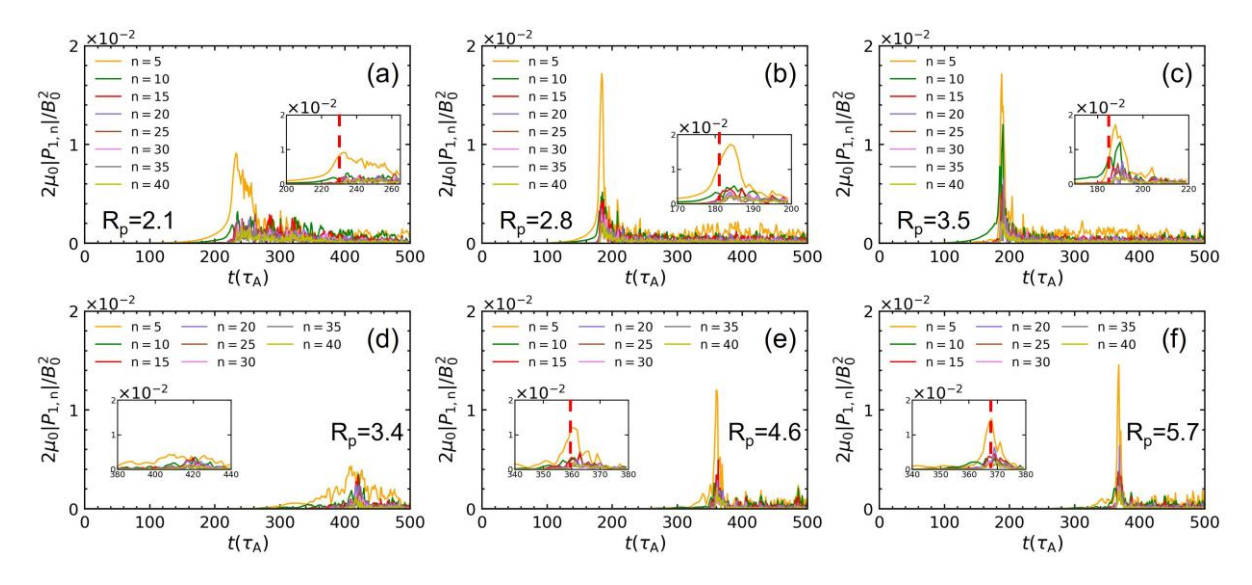


Fig. 3. Time evolutions of on-resonant modes when  $R_p = (a) 2.1$ , (b) 2.8 and (c) 3.5 in scenario LFS-X-point, and when  $R_p = (d) 3.4$ , (e) 4.6 and (f) 5.7 in scenario HFS-X-point. The insets in this figure include the period near ELM onset. The red dashed lines represent the time points of ELM onset, which are obtained based on the data of Fig. 2.

However, when Li pellets are injected from HFS X-point, the results are very different from those in scenario LFS-X-point. From Fig.  $3(d\sim f)$ , it can be found that regardless of the value of  $R_p$ , the existence of multiple nonlinear dominant modes is not observed. Additionally, in the cases of  $R_p = 4.6$  and 5.7, the nonlinear dominant n=5 mode does not undergo a secondary growth after ELM onset but rapidly decreases to a low level (which is comparable to other modes) within a very short time (only several time steps). Consequently, the corresponding pedestal energy loss then exhibits characteristics of P-B turbulence, as indicated by the purple and green curves in Fig. 2(b). As for the case of  $R_p = 3.4$ , it can be seen from Fig. 3(d) that although the n=5 mode is excited by nonlinear interaction and becomes dominant, its amplitude still remains at a low level, which is similar to other modes. As a result, only a small energy loss in the pedestal region is observed towards the end of the simulation time, as shown by the blue curve in Fig. 2(b).

# 3.3. Dependence of ELM size on pellet deposition amount

Finally, the dependence of ELM size on pellet deposition amount is discussed. Since the parameter  $R_p$  is only applicable for reflecting the pellet deposition amount in specific scenarios, it is inconvenient to directly compare the simulation results in scenarios of different poloidal injection positions by using  $R_p$ . Consequently, the total amount of pellet deposition is estimated from the initial change in normalized internal energy of the plasma system after pellet injection, which can be represented by the quantity  $\Delta E_{\rm tot,norm}$ . For its definition, please refer to [22]. By scanning  $R_p$ , Fig. 4 presents the variation of ELM size with  $\Delta E_{\rm tot,norm}$  for scenarios LFS-X-point, and HFS-X-point. Through comparison of the two scenarios, it can be clearly observed that the ELM triggering threshold

is smaller when lithium pellets are injected from the high-field side compared to the low-field side, which agrees well with the previous JOREK study [17]. Using the relationship between the initial change in normalized internal energy  $\Delta E_{\rm tot,norm}$  after pellet injection and pellet diameter  $d_{\rm p}$  from [22], the corresponding size thresholds  $d_{\rm p,thr}$  approximately 0.44–0.46 mm for scenario LFS-X-point, and 0.32–0.4 mm for scenario HFS-X-point, respectively.

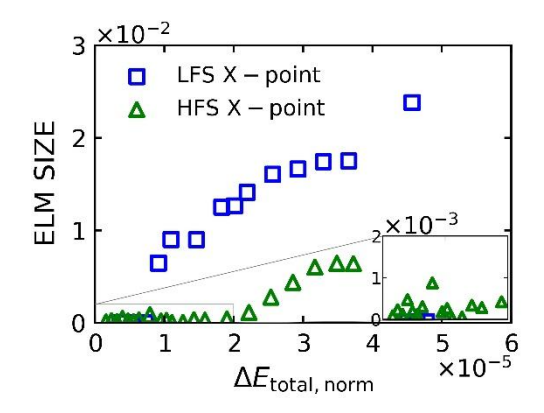


Fig. 4. ELM size at t = 500  $\tau_A$  versus initial change in normalized internal energy  $\Delta E_{tot,norm}$  in scenarios LFS-X-point and HFS-X-point.

In detail, for scenario LFS-X-point, when  $\Delta E_{\rm tot,norm}$  is below the threshold, the ELM sizes are zero; when the triggering threshold is exceeded, the ELM size is approximately proportional to  $\Delta E_{\rm tot,norm}$ , and the values are around 1% or higher. In contrast, the result for pellet injection from HFS X-point is different. It is found that in scenario HFS-X-point, when  $\Delta E_{\rm tot,norm} < 2 \times 10^{-6}$ , the ELM sizes are on the order of 0.1%, rather than zero. This finding indicates that when the poloidal injection position is on the high-field side, a wider parameter window exists for pellets, within which the injection of smaller-sized pellets can enhance edge particle transport without significantly degrading plasma confinement. Furthermore, it is observed from Fig. 4 that when  $\Delta E_{\rm tot,norm} > 2 \times 10^{-6}$ , the amplitudes of pellet-triggered ELMs remain smaller than those in scenario LFS-X-point, and with increasing  $\Delta E_{\rm tot,norm}$ , the pedestal energy loss eventually saturates.

# 4. CONCLUSIONS AND DISCUSSIONS

In the present paper, a BOUT++ three-field MHD code coupled with an impurity model is employed to investigate the physical mechanisms behind the process of pellet ELM triggering in the EAST experimental configuration, focusing on lithium pellet injection from different poloidal positions. The simulated poloidal injection positions included the low-field-side X-point (scenario LFS-X-point) and the high-field-side X-point (scenario HFS-X-point). For comparative analysis, the cases with comparable local pressure peak (LPP) after pellet injection are selected from scenarios LFS-X-point and HFS-X-point, although the Rp values, which indicate the pellet deposition amounts in each scenario, differ.

Nonlinear simulations shows that there exist significant differences in the characteristics of pellet-triggered ELMs in scenarios LFS-X-point and HFS-X-point. In scenario LFS-X-point, when the ELM triggering threshold is exceeded, the ELM evolution undergoes three distinct phases—fast crash, turbulent transport, and saturation—resulting in substantial energy loss from the pedestal region. The result is consistent with findings in [23] in which the pellet is injected from the poloidal position of OMP. In contrast, for scenario HFS-X-point, it is found that regardless of the LPP magnitude, the fast crash phase, associated with the most rapid energy loss, was negligible. The triggered ELM transitioned almost directly into and persisted in the turbulent transport phase (which characterizes slow energy loss) after an extended linear phase, resembling the turbulent crash mentioned in [29]. Consequently, the ELM loss in scenario HFS-X-point was considerably smaller than that in scenarios LFS-X-point.

In addition, the time evolution of the toroidal components of pressure perturbation is investigated. When pellets are injected from LFS X-point, it is found that in the cases of small LPP, the ELM is triggered by a single nonlinear dominant mode, which does not undergo a secondary growth during the fast crash phase after ELM onset but decays slowly with oscillations. The result indicates that the ELM crashes in small LPP cases are more similar to the conventional ELMs, differing from the turbulent ELMs observed in scenario OMP as referenced in [23].

Unlike scenario LFS-X-point, in scenario HFS-X-point, the existence of multiple dominant nonlinear modes is not observed, irrespective of LPP size. It is also found that for large LPP, although a nonlinear dominant mode emerges during the linear phase and finally trigger an ELM, its amplitude decays rapidly to a very low level, similar to other modes that failed to grow effectively.

Furthermore, the dependence of ELM size on the pellet deposition amount is also examined in this study. The comparison among the two scenarios clearly showed that the ELM triggering threshold was lower for high-field-side pellet injection compared to low-field-side X-point injection, which is in agreement with previous JOREK results [17]. Additionally, the trend of ELM size with pellet deposition amount in scenario HFS-X-point differs from that in scenario LFS-X-point: for small pellet injection, a broad parameter window is identified where ELM sizes remain around the order of 0.1%. The result suggests that the injection of a small pellet from HFS-X-point can enhance the edge particle transport without significantly degrading plasma confinement. This highlights the unique advantage of high-field-side pellet injection for ELM control.

The insights into the physical mechanisms of Li pellet triggering ELM obtained in this study are also expected to provide guidance for choosing the poloidal geometry in future D pellet injection experiments. However, further simulation and experimental investigations are necessary for validation.

#### **ACKNOWLEDGEMENTS**

This work is supported by the National Natural Science Foundation of China under Grant Nos. 12275040 and 12175275, the National Key R&D Program of China under Grant No. 2019YFE03030004, and Users with Excellence Program of Hefei Science Center CAS (2020HSC-UE010). It is also sponsored by the Youth Innovation Promotion Association, Chinese Academy of Sciences (Y2021114), and is partly supported by the US DOE under Contract No. DE-AC02-09CH11466. The authors also thank Supercomputing Center of Dalian University of Technology for providing part of computation resources, and Interdisciplinary and Collaborative Teams of CAS.

# 5. REFERENCES

- [1] ZOHM H., Edge localized modes (ELMs), Plasma Phys. Control. Fusion 38 (1996) 105-128.
- [2] LEONARD A.W., Edge-localized-modes in tokamaks, Phys. Plasma 21 (2014) 090501.
- [3] FEDERICI G., LOARTE A., STROHMAYER G., Assessment of erosion of the ITER divertor targets during type I ELMs, Plasma Phys. Control. Fusion 45 (2003) 1523-1547.
- [4] LANG P.T., CONWAY G.D., EICH T., et al., ELM pace making and mitigation by pellet injection in ASDEX Upgrade, Nucl. Fusion 44 (2004) 665-677.
- [5] BAYLOR L.R., COMMAUX N., JERNIGAN T.C., et al., Reduction of Edge-Localized Mode Intensity Using High-Repetition-Rate Pellet Injection in Tokamak H-Mode Plasmas, Phys. Rev. Lett. 110 (2013) 245001.
- [6] LANG P.T., FRIGIONE D., GÉRAUD A., et al., ELM pacing and trigger investigations at JET with the new ITER-like wall, Nucl. Fusion 53 (2013) 073010.
- [7] LUNSFORD R., HU J.S., SUN Z., et al., ELM frequency enhancement and discharge modification through lithium granule injection into EAST H-modes, Nucl. Fusion 58 (2018) 126021.
- [8] LUNSFORD R., SUN Z., MAINGI R., et al., Injected mass deposition thresholds for lithium granule instigated triggering of edge localized modes on EAST, Nucl. Fusion 58 (2018) 036007.
- [9] BORTOLON A., MAINGI R., MANSFIELD D.K., et al., High frequency pacing of edge localized modes by injection of lithium granules in DIII-D H-mode discharges, Nucl. Fusion 56 (2016) 056008.
- [10] KUKUSHKIN A.S., POLEVOIA A.R., PACHER H.D., et al., Physics requirements on fuel throughput in ITER, J. Nucl. Mater. 415 (2011) S497-S500.
- [11] MANSFIELD D.K., ROQUEMORE A.L., CARROLL T., et al., First observations of ELM triggering by injected lithium granules in EAST, Nucl. Fusion 53 (2013) 113023.
- [12] BORTOLON A., MAINGI R., MANSFIELD D.K., et al., Mitigation of divertor heat flux by high-frequency ELM pacing with non-fuel pellet injection in DIII-D, Nucl. Mater. Energy 12 (2017) 1030-1036.
- [13] LUNSFORD R., BORTOLON A., MAINGI R., et al., Supplemental ELM control in ITER through beryllium granule injection, Nucl. Mater. Energy 19 (2019) 34-41.
- [14] PÉGOURIÉ B., Review: Pellet injection experiments and modelling, Plasma Phys. Control. Fusion 49 (2007) R87-R160.

#### IAEA-CN-336/#3261

- [15] GÁL K., BELONOHY É., KOCSIS G., et al., Role of shielding in modelling cryogenic deuterium pellet ablation, Nucl. Fusion 48 (2008) 085005.
- [16] SUN J.Z., LIU L.J., SUN Z., et al., Numerical simulation of Li pellet ablation in the H-mode pedestal region, Fusion Eng. Des. 136 (2018) 834-838.
- [17] FUTATANI S., HUIJSMANS G., LOARTE A., et al., Non-linear MHD modelling of ELM triggering by pellet injection in DIII-D and implications for ITER, Nucl. Fusion 54 (2014) 073008.
- [18] FUTATANI S., PAMELA S., GARZOTTI L., et al., Non-linear magnetohydrodynamic simulations of pellet triggered edge-localized modes in JET, Nucl. Fusion 60 (2020) 026003.
- [19] CATHEY A., HOELZL M., FUTATANI S., et al., Comparing spontaneous and pellet-triggered ELMs via non-linear extended MHD simulations, Plasma Phys. Control. Fusion 63 (2021) 075016.
- [20] FUTATANI S., CATHEY A., HOELZL M., et al., Transition from no-ELM response to pellet ELM triggering during pedestal build-up—insights from extended MHD simulations, Nucl. Fusion 61 (2021) 046043.
- [21] GAO F., SUN J.Z., SUN Z., et al., Numerical simulation of Li-pellet injection experiments for ELM-pacing in EAST, Nucl. Fusion 60 (2020) 066022.
- [22] LI M., XIA T.Y., SUN Z., et al., Simulation of triggering and evolution of ELM by pellet injection in EAST under BOUT++framework, Nucl. Fusion 64 (2024) 086061.
- [23] LI M., SUN Z., SUN J.Z., et al., Simulation of Li-pellet triggered ELMs in EAST with an impurity model implemented under BOUT++ framework, Nucl. Fusion 65 (2025) 026007.
- [24] Xi P.W., XU X.Q., XIA T.Y., et al., Impact of a large density gradient on linear and nonlinear edge-localized mode simulations, Nucl. Fusion 53 (2013) 113020.
- [25] XU X.Q., UMANSKY M. V., DUDSON B., et al., Boundary Plasma Turbulence Simulations for Tokamaks, Commun. Comput. Phys. 4 (2008) 949-979.
- [26] XU X.Q., DUDSON B., SNYDER P.B., et al., Nonlinear Simulations of Peeling-Ballooning Modes with Anomalous Electron Viscosity and their Role in Edge Localized Mode Crashes, Phys. Rev. Lett. 105 (2010) 175005.
- [27] XIA T.Y., XU X.Q., Five-field simulations of peeling-ballooning modes using BOUT++ code, Phys. Plasmas 20 (2013) 052102.
- [28] XIA T.Y., XU X.Q., XI P.W., Six-field two-fluid simulations of peeling-ballooning modes using BOUT++, Nucl. Fusion 53 (2013) 073009.
- [29] XI P.W., XU X.Q., DIAMOND P.H., Phase Dynamics Criterion for Fast Relaxation of High-Confinement-Mode Plasmas, Phys. Rev. Lett. 112 (2014) 085001.